PHYSICAL REVIEW B **82**, 064110 (2010)

Structure of siderite $FeCO_3$ to 56 GPa and hysteresis of its spin-pairing transition

Barbara Lavina,[1] Przemyslaw Dera,[2] Robert T. Downs,[3] Wenge Yang,[4,5] Stanislav Sinogeikin,[4] Yue Meng,[4] Guoyin Shen,[4] and David Schiferl[1]

[1]*High Pressure Science and Engineering Center and Department of Physics and Astronomy, University of Nevada, Las Vegas, Nevada 89154, USA*

[2]*GSECARS, University of Chicago, Building 434A, 9700 South Cass Avenue, Argonne, Illinois 60439, USA*

[3]*Geosciences, University of Arizona, Tucson, Arizona 85721-0077, USA*

[4]*HPCAT, Carnegie Institution of Washington, Building 434E, 9700 South Cass Avenue, Argonne, Illinois 60439, USA*

[5]*HPSynC, Carnegie Institution of Washington, Building 401, 9700 South Cass Avenue, Argonne, Illinois 60439, USA*

(Received 20 May 2010; published 23 August 2010)

The structure of siderite, $FeCO_3$, was determined to 56 GPa, beyond the spin-pairing transition of its iron *d* electrons. Fe^{2+} in the siderite structure is in the high-spin state at low pressures and transforms to the low-spin (LS) state over a narrow pressure range, 44 to 45 GPa, that is concomitant with a shrinkage of the octahedral bond distance by 4%, and a volume collapse of 10%. The structural rearrangements associated with the electronic transition are nearly isotropic in contrast with other properties of siderite, which mostly are highly anisotropic. Robust refinements of the crystal structure from single-crystal x-ray diffraction data were performed at small pressure intervals in order to accurately evaluate the variation in the interatomic distances and to define the geometry of the carbonate hosting LS-Fe^{2+}. Thermal vibrations are remarkably lowered in the LS-Sd as shown by atomic displacement parameters. The formation of like-spin domains at the transition shows a hysteresis of more than 3 GPa, compatible with a strong cooperative contribution of neighboring clusters to the transition.

DOI: 10.1103/PhysRevB.82.064110 PACS number(s): 61.66.−f, 75.30.Fv, 62.50.−p, 91.60.Ba

I. INTRODUCTION

The study of the high-pressure behavior of Fe-bearing carbonates is relevant to the deep Earth carbon cycle, and provides an ideal case study of the effect of the pressure-induced spin pairing of ferrous iron *d* electrons at mantle conditions. The most likely candidate for a deep Earth carbonate is an iron-bearing magnesite, $MgCO_3$.[1–4]

The structure of the calcite-group rhombohedral carbonates, the iron member of which is siderite, has been known since the earliest days of structural determinations. Siderite exhibits space-group symmetry $R\bar{3}c$, where, in the hexagonal setting, iron is located at the cell origin (6*b*), oxygen is at *x*, 0, 1/4 (18*e*), and carbon is at 0,0,1/4 (6*a*).[5] The atomic arrangement can be envisioned as a distorted rocksalt structure with Fe as the cation and CO_3 groups as the anions. The CO_3 groups form planes perpendicular to the *c* axis with Fe occupying the interstitial octahedral voids between the planes. No bond or polyhedral edge is parallel to the *c* axis.

The spin-pairing transition of Fe^{2+} in siderite (Sd) was first discovered by means of x-ray emission spectroscopy,[6] then modeled with first-principles calculations,[7] and recently its effect on cell parameters and density was investigated by means of single crystal x-ray diffraction.[8] In mantle minerals, the spin-pairing transition occurs over a wide pressure interval eventually through intermediate states as a consequence of high temperature, variability in iron content, and distortion of the iron coordination (e.g., Refs. 9–12). Given the complexity of natural systems, it is necessary to fully understand and parameterize the effect of *T*, *P*, composition, and structure on the occurrence and width of the spin transition. Siderite provides a meaningful case study because (i) rhombohedral carbonates are among the few minerals where mixed valence substitutions are negligible; (ii) symmetry constraints impose the six metal-ligand bond distances of the Fe^{2+} coordination sphere to be equal because the metal is located on an inversion center such that only trigonal distortion of the octahedron is allowed; (iii) iron polyhedra only share corners, the Fe-Fe interaction is relatively weak compared to wüstite, for instance; (iv) along with diamond, the calcite-group minerals, form the most perfect, defect-free crystals to be found in nature. In summary, some of the factors complicating our understanding of the behavior of the electronic phase transition in mantle minerals, such as mixed iron valence and sites of variable coordination and distortion, can be ignored in siderite.

II. EXPERIMENTAL

High pressure was generated using a four-pin opposing plate diamond-anvil cell equipped with Boehler-Almax anvils[13] of 300 μm tip diameter and 70° aperture. A 120 μm diameter hole was drilled in a Re foil that had been indented to ~40 μm thickness and used as a sample chamber between the anvils. A 12×17 μm^2 rhombohedral cleavage fragment with perfectly parallel surfaces, about 7 μm thick, of natural siderite from Invigtut, Greenland was placed at the center of one anvil tip with a small ruby sphere, which was used for online pressure measurement in the gas loading system, and gold powder (Fig. 1) used for pressure calibration. After collecting data at ambient conditions, the sample chamber was filled with Ne at 172 MPa using the GSECARS/COMPRES gas loading system.[14] Single-crystal diffraction data were collected using the rotation method (ω axis) at three stations of the APS, Argonne National Labora-

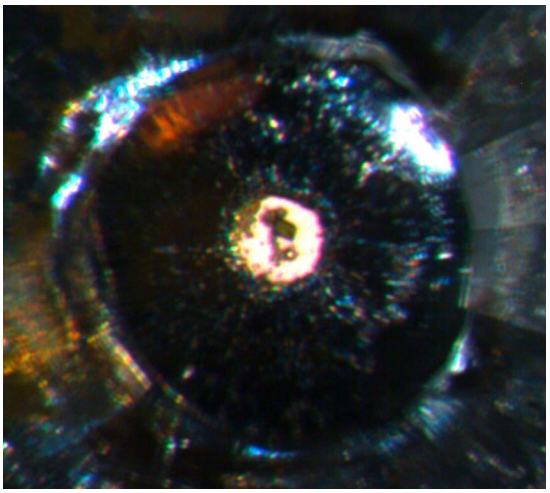

FIG. 1. (Color online) The sample chamber at the center of the cupped anvils shrank to a diameter of ~60 μm at 55 GPa. Below the crystal, a cleavage rhombohedron, is a ruby sphere while the irregular dark material is fine gold powder. Crystal and pressure gauges are embedded in Ne.

tory. Most of the data were collected at the station 16BMD, HPCAT. Additional data were collected at stations 16IDB and 13IDD of HPCAT and GSECARS, respectively, with the aim of testing the reliability and reproducibility of the results with changing beamline setup. The experimental conditions at the three stations are summarized in Table I. Pressure was calculated from the equation of state of gold.[15] Diffraction data were collected at 30 different pressures in the range of 0–56 GPa at room temperature, including three steps in decompression. Fine CeO_2 standard powder (NIST) was used for detector calibration with the software FIT2D.[16] Using the software GSE_ADA,[17] integrated intensities and two peak coordinates, 2θ and χ, were extracted from the 70° wide angle scan exposure while a third coordinate, ω, was determined from step scan data of 1° intervals. GSE_ADA was also used to apply the Lorentz and polarization corrections, the latter empirically calibrated. The determination of the orientation matrix and the refinement of the lattice parameters from more than 100 unique d-spacing values were performed with the software RSV.[17] For the structural analysis, saturated and overlapping peaks as well as those at the limit of the angular scan range, were discarded. Absorption of the anvils, although very small, was taken into account; absorption of the crystal with a μr of 0.13 is negligible. Structural refinements were performed with SHELXL97,[18] data are reported in Ref. 19.

TABLE I. Experimental conditions at the three stations of the APS used to collect diffraction data.

Station	16BMD	16IDB	13IDD
Energy (keV)	33.00	30.49	37.07
Beam size (FWHM) horizontal and vertical (μm)	5–10	5–5	5–5
Detector	IP	CCD and IP	CCD

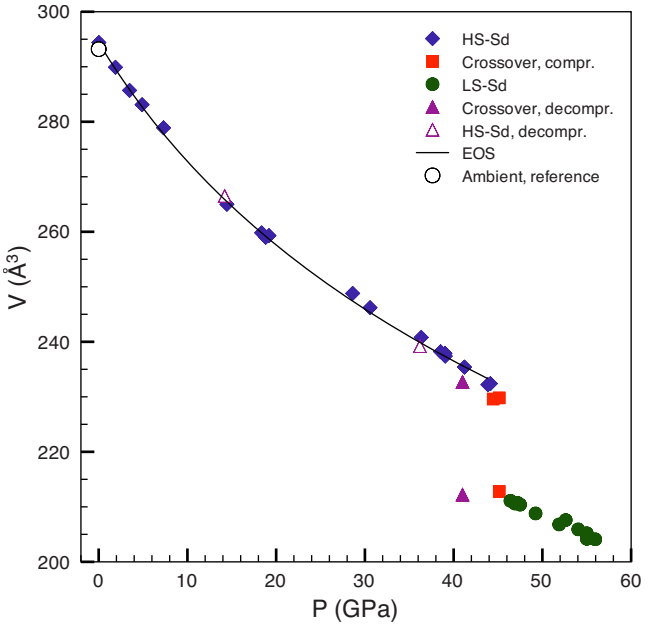

FIG. 2. (Color online) Unit-cell volume of siderite. Diamonds: HS-Sd, compression; circles: LS-Sd; squares: crossover, compression; solid triangles: crossover, decompression; empty triangles: HS-Sd decompression; empty circle: value from the literature (Ref. 20).

III. RESULTS AND DISCUSSION

A. Unit-cell compressibility

The siderite specimen is close to end-member composition as can be inferred by the close match of the lattice parameters measured at ambient pressure with those from the literature (Fig. 2).[20] The bulk modulus of HS-Sd, calculated by fitting the pressure volume data between 0 and 43.9 GPa to a third-order Birch-Murnaghan equation of state, is K_0 =110(2) GPa with K_0'=4.6(2), and K_0=117.1(8) GPa with K_0' fixed at 4, in excellent agreement with the literature, K_0 =117(1) GPa with K_0'=4, recorded to 8.9 GPa.[21] The c axis is much more compressible than the a axis [Fig. 3(a)], a behavior common to the series of rhombohedral carbonates.[22,23] The value of K_0 and K_0' (Table II) obtained for the two cell parameters, are in reasonable agreement with those found for the isostructural magnesite.[24]

As previously reported, the spin pairing in siderite is manifested by an abrupt volume contraction of 10% (Ref. 7) and an absorption increase in the visible range,[8] features that allows to distinguish between siderite with iron in the high-spin state (HS-Sd) from siderite with iron in the low-spin state (LS-Sd).

The a-axis shrinkage (3%) with the spin transition is comparable to the c-axis shrinkage (4%), the nearly isotropic deformation of the cell is in contrast with the strongly anisotropic behavior with pressure. The a cell contracts by 4.5% between 0 and 45 GPa while the c axis contracts by 14.5%. Even if we do not observe the change in cell distortion suggested by first-principles calculations,[7] we stress that the continuous trend of the c/a ratio with pressure [Fig. 3(a)] is in unexpected contrast with the discontinuous distortion in-

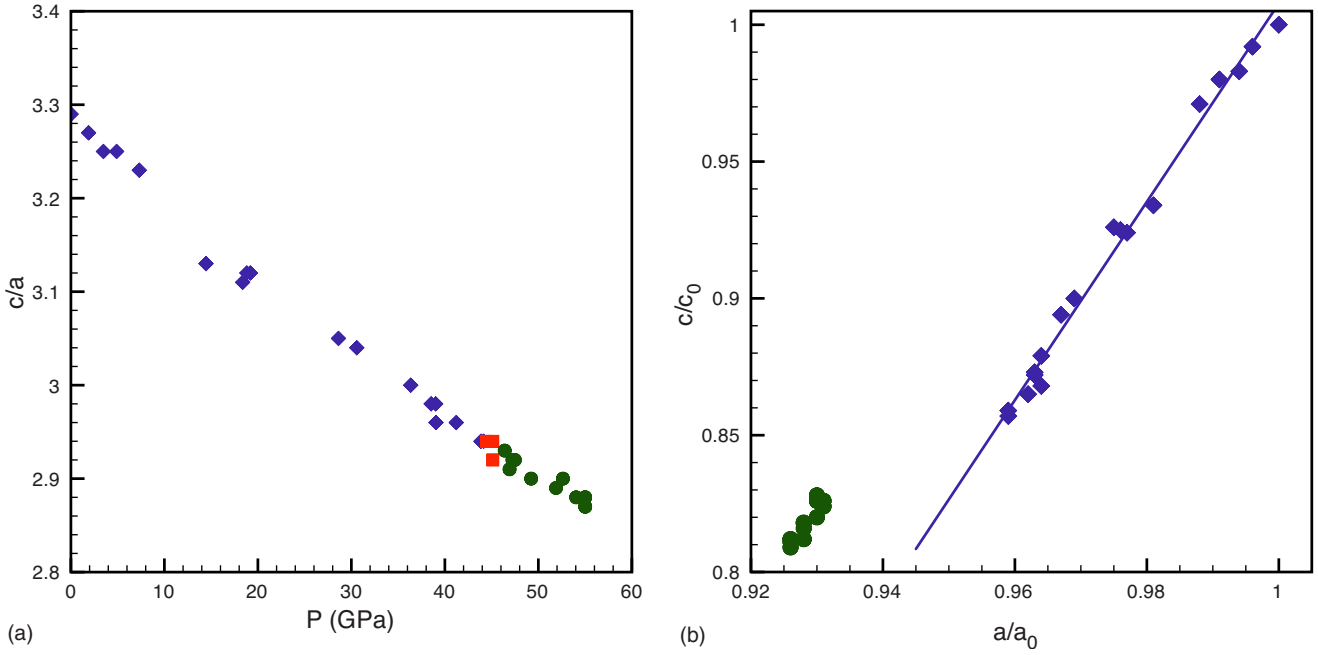

FIG. 3. (Color online) Ratio of cell parameters as a function of (a) pressure and (b) their relative variation.

duced by the spin transition. Figure 3(b) emphasizes the large change in the length of the a axis at the spin transition in opposition to its stiffness during compression, as well as the discontinuity in the relative variations in the two axes. The volumes measured in decompression at 36 and 14 GPa, closely match the compression curve, suggesting that siderite fully recovered to the high-spin state below 36 GPa.

B. Structural refinements

The refinements typically use about 100 structure factors, reduced to 30 after merging the symmetry equivalents. Based on the disagreement between equivalent reflections and/or between observed and calculated structure factors, about five reflections were omitted from each of the final refinements. The refined parameters are the scale factor, the oxygen fractional coordinate and the isotropic displacement parameters of Fe and O; the displacement parameter of C was fixed at 0.005 $Å^2$. The correction for extinction was unnecessary, as should be expected for a small crystal, particularly after a small mosaicity increase under pressure. Most refinements show very satisfactory statistical parameters and uniform distribution of errors with respect to the 2θ angle and the intensity. The measurement of structure factors of small crystals at high pressure presents unique challenges. Variable volume of illuminated crystal during rotation, limited coverage, and redundancy, as well as the effects of diamond diffraction,[25] are the major concerns. In order to test the robustness of our refinements, we compared the result obtained from data collected at different χ angles, beam size and energy and detector type. A detailed discussion will be presented elsewhere, however the inspection of results (Ref. 19) shows that all refinements are in excellent agreement.

The oxygen fractional coordinate, x(O), is the most important result from the refinements because, together with the cell parameters, it allows the complete description of the geometry of rhombohedral carbonates. The increase in the oxygen parameter with pressure (Fig. 4) is a result of the increase in the relative size of the incompressible CO_3 unit with respect to the octahedral face perpendicular to the c axis.

Displacement parameters are the least constrained result of the refinements, nevertheless, values are moderately scattered, physically reasonable and statistically significant. Results from data collection strategies and processing tests (triangles in Fig. 5) are slightly more scattered but in reasonable agreement with the data collected at 16BMD; greater scatter-

TABLE II. Bulk moduli calculated for HS-Sd using the third-order BM equation of state and relative variation in parameters with the change in spin state ($\Delta x/x\%$). For linear quantities, moduli were fitted using the cubic values (Ref. 32). (*): fitting performed with K_0' constraint to the value 4, reported in square brackets.

	V	V^*	a-axis	c-axis	Fe^{2+}-O	O-$O_{\|}$	O-O_L	O-O_T
x_0	294.4(3) $Å^3$	294.4(3) $Å^3$	4.694(1) Å	15.43(1) Å	2.147(2) Å	3.094(2) Å	2.978(4) Å	2.916(2) Å
K_0 (GPa)	110(2)	117.1(8)	164(7)	63(6)	97(6)	79(2)	110(20)	78(2)
K_0'	4.6 (2)	[4]	15(1)	2.5 (3)	4.9 (6)	2.9 (1)	18 (5)	2.6 (1)
$\Delta x/x$ (%)	10.4		2.9	4.2	4.4	4.3	4.5	3.4

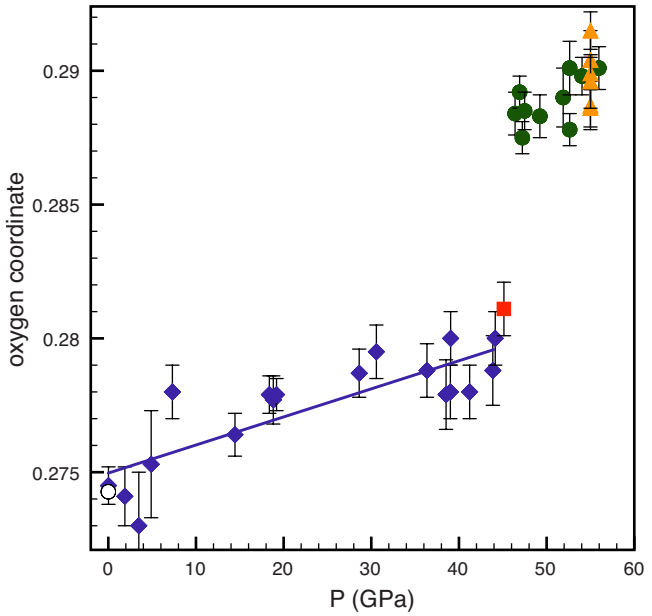

FIG. 4. (Color online) Oxygen fractional coordinate as a function of pressure. Diamond: HS-Sd; circles: LS-Sd; squares: crossover; triangles: results from stations 16IDB and 13IDD; empty circle: literature value (Ref. 20).

ing of values for the O displacement parameters is due to its lower scattering power. Isotropic displacement parameters of Fe and O are nearly constant in HS-Sd and drop by more than 20% after the transition to the low-spin state (Fig. 5). Thermal vibrations appear hindered in the dense LS-Sd.

C. Peak splitting at the spin transition

In the entire pressure range, except for the spin crossover, peaks are sharp and their profiles symmetrical [Fig. 6(a)]. A subtle variation in the peak shape, not involving a significant increase in the peak width, is noticeable at 44.1 GPa [Fig. 6(b)]. The loss of peak shape symmetry suggests the development of weak strain, the first precursor of the electronic phase transition. At 44.5 and 45.1 GPa, peaks are split in 2θ [Fig. 6(c)]. The formation of like-spin domains was observed at slightly lower pressure, 43 GPa, in a previous experiment[8] likely due to less hydrostatic conditions as evidenced by broader peaks. The stronger component, at lower 2θ, corresponds to a volume that matches the compressibility curve of HS-Sd; the d spacing of the weaker component allows to calculate a volume that well corresponds to the compressibility curve of LS-Sd (Fig. 2). The two components are fully separated [see red peak profile in Fig. 6(e)], excluding any intermediate state at ambient temperature. The rather irregular shape of most of peaks at the transition is a response of the strain between domains of different volume. After the transition, peaks fully recover their original shapes, the dramatic volume change, and the strain between domains did not induce appreciable plastic deformations. Guided by the fading of the color shown by LS-Sd,[8] we could observe the development of domains also in decompression, at 41 GPa, a pressure 3 GPa lower than the first sign of onset of the transition in compression.

The formation of like-spin domains, the hysteresis of the transition, and the shift of the transition to higher pressure in diluted systems[26] are characteristic of systems where the spin transitions have a strong cooperative component through elastic interactions[27] where the strain is induced locally by ions of different size. The hysteresis evidences a first-order character of the spin transition originating in the intersite coupling.[28] The development of distinct spin domains has been observed in several temperature and light-induced spin transitions[29,30] and could be observed in this study because of the quasihydrostatic conditions and the high resolution of the technique used.

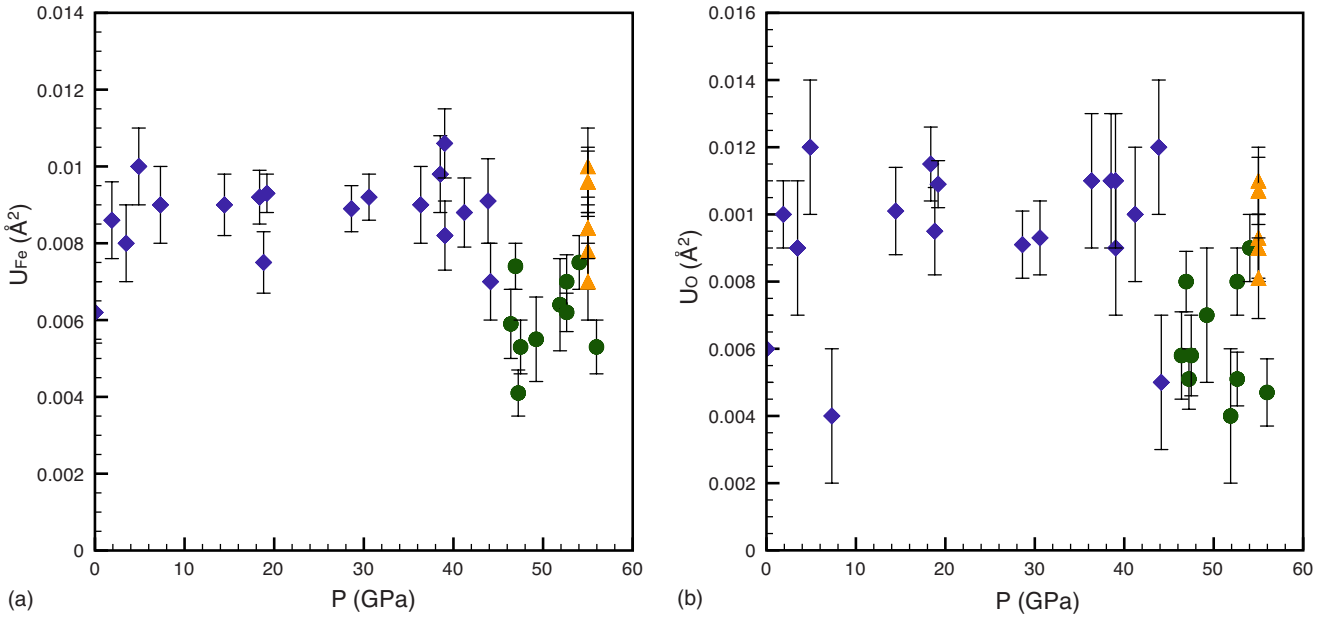

FIG. 5. (Color online) Refined isotropic displacement parameters of (a) iron and (b) oxygen as a function of pressure.

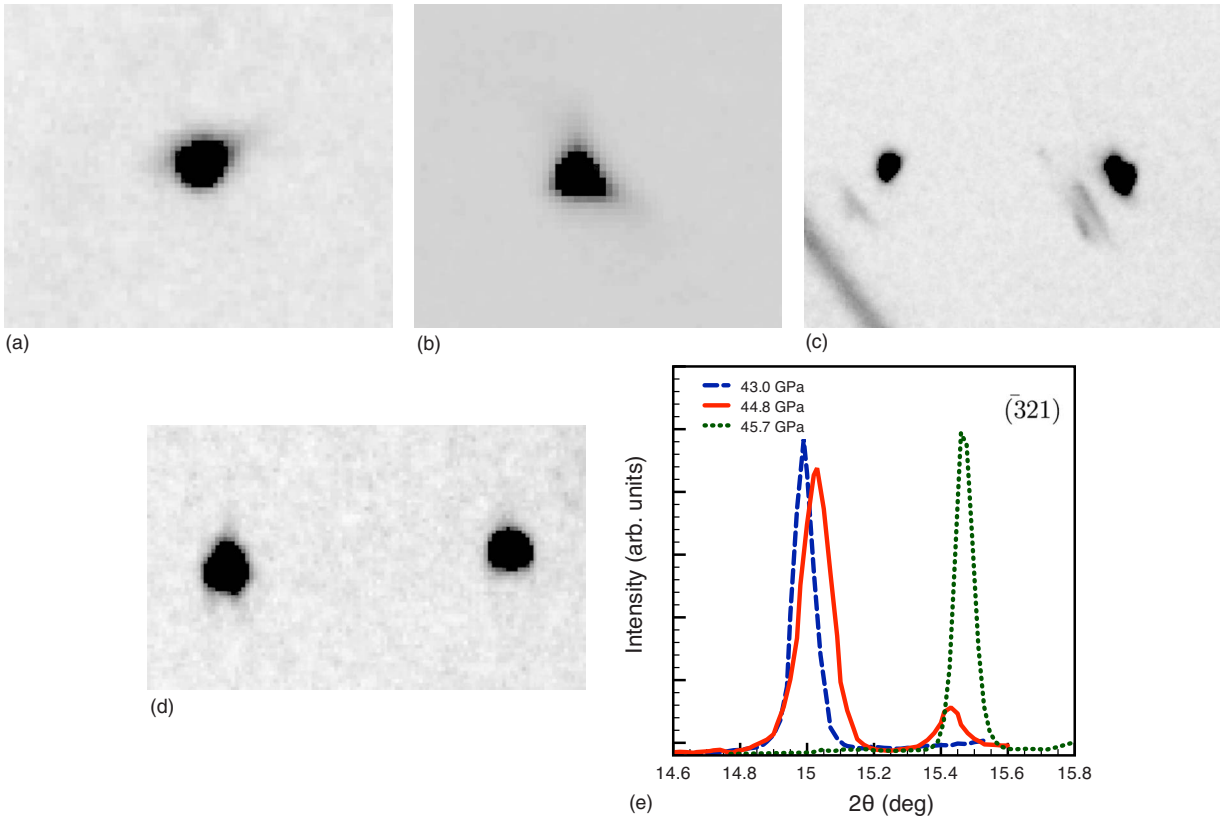

FIG. 6. (Color online) Peak shape at different pressures, (a): 43.86 GPa, (b): 44.14 GPa, (c): 45.13 GPa, (d): 46.40 GPa, and (e) comparison of the profile of a peak before, after and at the spin transition.

D. Interatomic distances and geometry of LS siderite

The short, strong C-O bond shows a decrease by only 0.03 Å over 45 GPa [Fig. 7(a)], in good agreement with the results for the isostructural magnesite, $MgCO_3$, obtained by means of IR spectroscopy.[31] Within uncertainty, the bond shows a linear variation with pressure within HS-Sd. The compressibility of the octahedral bond length [Fig. 7(b)] was evaluated by fitting its cube against the third-order Birch-Murnaghan equation of state,[32] obtaining K_0=97(6) GPa and K_0'=4.9(6). The octahedral edges (the edge perpendicular to the c axis, O-O_L and the edge oblique to the c axis, O-O_T) show very different compressibility (Table II) causing a change in the octahedral distortion from trigonally elon-

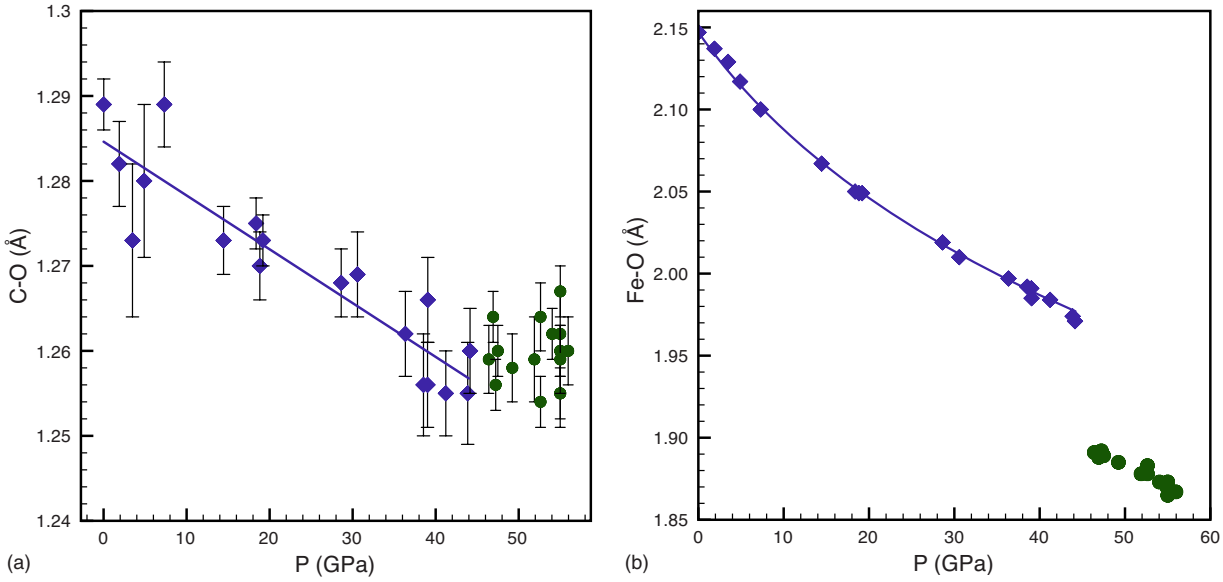

FIG. 7. (Color online) Compressibility of the (a) carbon-oxygen and of the (b) iron-oxygen bonds.

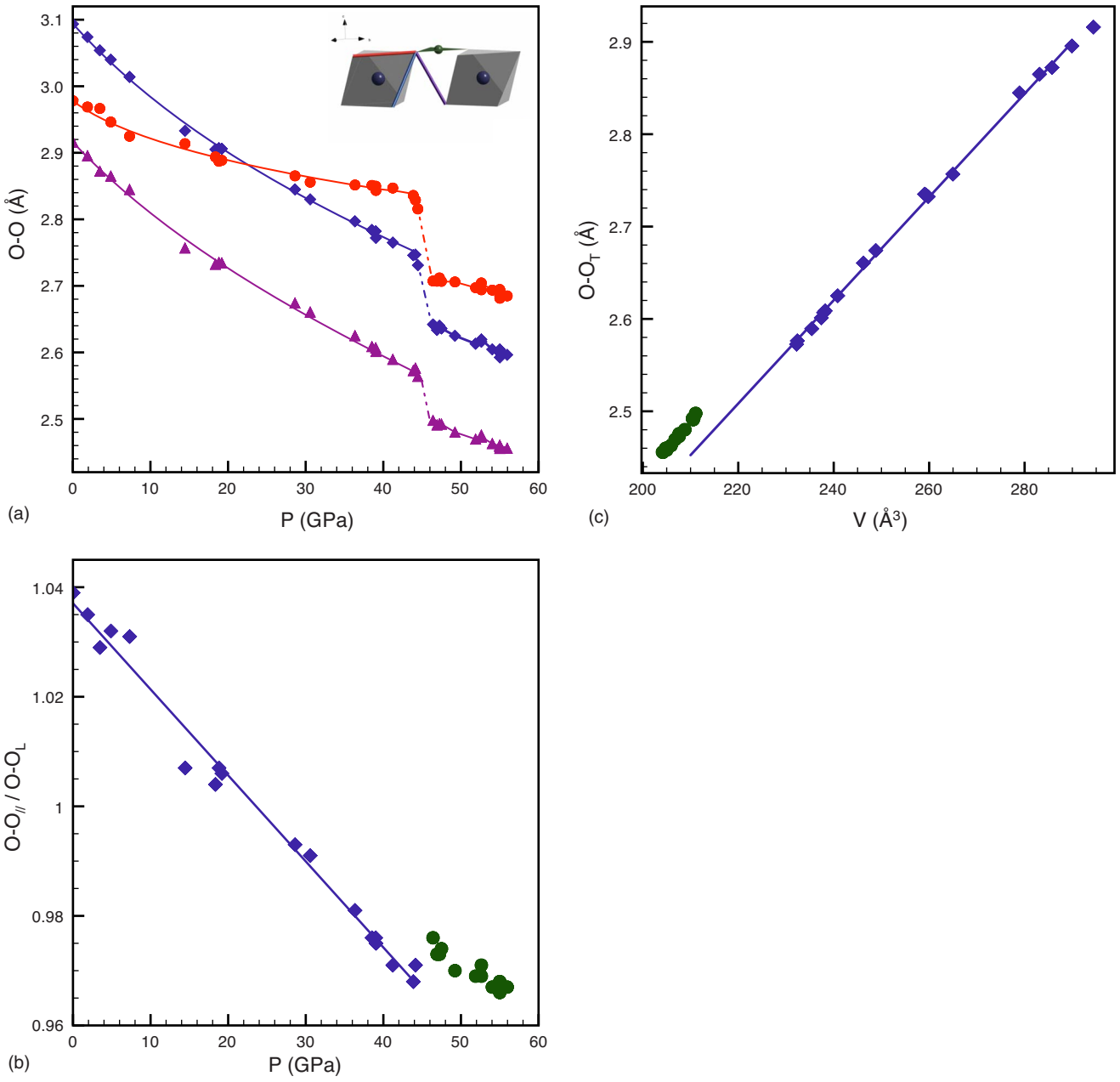

FIG. 8. (Color online) (a) Oxygen-oxygen distances, (b) distortion of the Fe coordination site as a function of pressure and (c) nonpolyhedral oxygen-oxygen distance as a function of volume. In the inset in (a), the atomic separations are color coded as in the plot: circles: O-O_L, diamonds: O-$O_{\|}$, triangles: O-O_T.

gated to trigonally compressed through a regularization at about 23 GPa [Figs. 8(a) and 8(b)].

After the spin transition, the C-O bond length shows a small but appreciable lengthening, that can be envisioned as due to a stress release of the C-O bond induced by the shrinkage of the *M*-O bond. Resembling the behavior of the cell parameters, the octahedral edges show a similar shrinkage with the transition that contrasts their remarkably anisotropic response to external pressure within HS-Sd. As a consequence, the octahedron is slightly more regular at pressure above the transition than it was at pressures lower than the transition [Fig. 8(b)]. The unusually short nonpolyhedral oxygen-oxygen distance (O-O_T) (Ref. 20) remains shorter than the octahedral edges in the entire pressure range [Fig. 8(a)] however its value is not as small as could be expected from its volume dependence in HS-Sd [Fig. 8(c)]. In summary, LS-Sd show a geometry that cannot be simply predicted from the trends observed for the HS-Sd, nor from ionic sizes considerations. Perhaps the minimization of the distortion of the LS-Fe^{2+} can explain the unusual high shrinkage at the crossover of the *a* axis, in spite of a small expansion of the CO_3 unit.

IV. CONCLUSIONS

This study presents detailed observations of the pressure-induced spin-pairing transition obtained indirectly by means

of single-crystal x-ray diffraction. The spin pairing occurs over a narrow pressure range through the development of spinlike domains, the phenomenon shows hysteresis in decompression, interpreted as due to a strong cooperative component of the spin pairing, similarly to that observed in a number of temperature and light-induced transitions. The nearly isotropic structural rearrangement after the spin transition is in marked contrast with the strong anisotropy of many other physical properties in siderite. The rearrangement of the structure following the spin transition might be driven by minimization of octahedral distortion and of shrinkage of the nonpolyhedral $O\text{-}O_T$ distance, particularly short at ambient conditions.

ACKNOWLEDGMENTS

The UNLV High Pressure Science and Engineering Center (HiPSEC) is supported by DOE-NNSA under Cooperative Agreement No. DE-FC52-06NA262740. Diffraction data were collected at HPCAT (Sector 16), Advanced Photon Source (APS), Argonne National Laboratory. HP-CAT is supported by DOE-BES, DOE-NNSA, NSF, and the W.M. Keck Foundation. GeoSoilEnviroCARS is supported by the National Science Foundation—Earth Sciences (Grant No. EAR-0622171) and Department of Energy—Geosciences (Grant No. DE-FG02-94ER14466). The APS is supported by DOE-BES under Contract No. DE-AC02-06CH11357. This work was supported by the Carnegie-DOE Alliance Center under cooperative Agreement No. DE FC52-08NA28554. HPSynC is supported as part of EFree, an Energy Frontier Research Center funded by the U.S. Department of Energy, Office of Science, Office of Basic Energy Sciences under Award No. DE-SC0001057. We thankfully acknowledge the Department of Mineral Sciences, Smithsonian Institution for providing sample NMNH 17893-2. We thank GSECARS and COMPRES for the use of the Gas Loading System. Oliver Tschauner, James Norton, and Amo Sanchez are gratefully acknowledged for the development of the high pressure device used in this experiment.

[1] C. Biellmann, P. Gillet, F. Guyot, J. Peyronneau, and B. Reynard, Earth Planet. Sci. Lett. **118**, 31 (1993).
[2] M. Isshiki, T. Irifune, K. Hirose, S. Ono, Y. Ohishi, T. Watanuki, E. Nishibori, M. Takata, and M. Sakata, Nature (London) **427**, 60 (2004).
[3] Y. Seto, D. Hamane, T. Nagai, and K. Fujino, Phys. Chem. Miner. **35**, 223 (2008).
[4] W. R. Panero and J. E. Kabbes, Geophys. Res. Lett. **35**, L14307 (2008).
[5] W. Bragg, Proc. R. Soc. London **89**, 248 (1913).
[6] A. Mattila, T. Pylkkanen, J.-P. Rueff, S. Huotari, G. Vanko, M. Hanfland, M. Lehtinen, and K. Hamalainen, J. Phys.: Condens. Matter **19**, 386206 (2007).
[7] H. Shi, W. Luo, B. Johansson, and R. Ahuja, Phys. Rev. B **78**, 155119 (2008).
[8] B. Lavina, P. Dera, R. T. Downs, V. Prakapenka, M. Rivers, S. Sutton, and M. Nicol, Geophys. Res. Lett. **36**, L23306 (2009).
[9] J.-F. Lin, G. Vanko, S. D. Jacobsen, V. Iota, V. V. Struzhkin, V. B. Prakapenka, A. Kuznetsov, and C.-S. Yoo, Science **317**, 1740 (2007).
[10] J.-F. Lin *et al.*, Nat. Geosci. **1**, 688 (2008).
[11] J. Li, V. Struzhkin, H. Mao, J. Shu, R. Hemley, Y. Fei, B. Mysen, P. Dera, V. Prakapenka, and G. Shen, Proc. Natl. Acad. Sci. U.S.A. **101**, 14027 (2004).
[12] C. McCammon, I. Kantor, O. Narygina, J. Rouquette, U. Ponkratz, I. Sergueev, M. Mezouar, V. Prakapenka, and L. Dubrovinsky, Nat. Geosci. **1**, 684 (2008).
[13] R. Boehler and K. De Hantsetters, High Press. Res. **24**, 391 (2004).
[14] M. Rivers, V. B. Prakapenka, A. Kubo, C. Pullins, C. M. Holl, and S. D. Jacobsen, High Press. Res. **28**, 273 (2008).
[15] Y. Fei, A. Ricolleau, M. Frank, K. Mibe, G. Shen, and V. Prakapenka, Proc. Natl. Acad. Sci. U.S.A. **104**, 9182 (2007).
[16] A. Hammersley, S. Svensson, A. Thompson, H. Graafsma, A. Kvick, and J. Moy, Rev. Sci. Instrum. **66**, 2729 (1995).
[17] P. Dera, B. Lavina, L. A. Borkowski, V. B. Prakapenka, S. R. Sutton, M. L. Rivers, R. T. Downs, N. Z. Boctor, and C. T. Prewitt, Geophys. Res. Lett. **35**, L10301 (2008).
[18] G. M. Sheldrick, Acta Crystallogr., Sect. A: Found. Crystallogr. **64**, 112 (2008).
[19] See supplementary material at http://link.aps.org/supplemental/10.1103/PhysRevB.82.064110 for experimental data.
[20] H. Effenberger, K. Mereiter, and J. Zemann, Z. Kristallogr. **156**, 233 (1981).
[21] J. Z. Zhang, I. Martinez, F. Guyot, and R. J. Reeder, Am. Mineral. **83**, 280 (1998).
[22] J. Z. Zhang and R. J. Reeder, Am. Mineral. **84**, 861 (1999).
[23] N. Ross, Am. Mineral. **82**, 682 (1997).
[24] K. D. Litasov, Y. Fei, E. Ohtani, T. Kuribayashi, and K. Funakoshi, Phys. Earth Planet. Inter. **168**, 191 (2008).
[25] J. Loveday, M. McMahon, and R. J. Nelmes, J. Appl. Crystallogr. **23**, 392 (1990).
[26] B. Lavina, P. Dera, R. T. Downs, O. Tschauner, W. Yang, O. Shebanova, and G. Shen, High Press. Res. **30**, 224 (2010).
[27] A. Hauser, J. Jeftic, H. Romstedt, R. Hinek, and H. Spiering, Coord. Chem. Rev. **190-192**, 471 (1999).
[28] W. Nicolazzi, S. Pillet, and C. Lecomte, Phys. Rev. B **78**, 174401 (2008).
[29] C. Chong, F. Varret, and K. Boukheddaden, Phys. Rev. B **81**, 014104 (2010).
[30] N. Huby, L. Guerin, E. Collet, L. Toupet, J. Ameline, H. Cailleau, T. Roisnel, T. Tayagaki, and K. Tanaka, Phys. Rev. B **69**, 020101(R) (2004).
[31] J. Santillan, K. Catalli, and Q. Williams, Am. Mineral. **90**, 1669 (2005).
[32] R. J. Angel, *High-Temperature and High-Pressure Crystal Chemistry* (Mineralogical Society of America and the Geochemical Society, Washington, DC, 2001), p. 35.

P#	P0	P1	P2	P3	P4	P5	P6	P7	P8	P9	P10	P11	P12	P13
Station	16BMD	16BMD	16BMD	16BMD	16BMD	16BMD	16BMD	16BMD	16BMD	16BMD	16BMD	16BMD	16BMD	16BMD
χ angle	χ a	χ a	χ a	χ a	χ a	χ a	χ a	χ a	χ a	χ a	χ a	χ a	χ a	χ a
P (GPa)	0.02 (2)	1.89 (4)	3.48 (3)	4.89 (1)	7.31 (11)	14.4 (1)	18.37 (10)	18.82 (8)	19.19 (12)	28.62 (12)	30.6 (2)	36.3 (2)	38.5 (2)	39.05 (2)
a (Å)	4.694 (1)	4.676 (1)	4.664 (1)	4.650 (2)	4.637 (2)	4.607 (1)	4.587 (1)	4.575 (3)	4.579 (3)	4.548 (4)	4.539 (2)	4.527 (2)	4.519 (2)	4.523 (2)
c (Å)	15.43 (1)	15.310 (13)	15.168 (12)	15.12 (2)	14.98 (2)	14.415 (11)	14.258 (10)	14.29 (2)	14.28 (3)	13.89 (2)	13.80 (2)	13.57 (2)	14.47 (1)	13.40 (1)
V (Å^3)	294.4 (3)	289.9 (4)	285.7 (3)	283.1 (6)	278.9 (6)	265.0 (3)	259.8 (3)	259.0 (7)	259.3 (9)	248.8 (8)	246.2 (6)	240.8 (6)	238.2 (4)	237.4 (4)
N_{all}	134	145	141	118	119	100	128	124	132	108	101	88	104	99
N_{ind}	41	45	36	36	34	32	39	43	37	36	37	36	37	29
R_{int}	13.6	13.2	26	17	20	6.8	8.8	9.1	11	9.7	8.6	11.6	8	8.1
R_{all}	3.4	4.5	7.8	4.5	5.2	3.1	3.8	4.1	2.9	4.4	2.9	4.4	4.7	3.7
wR2	8.6	11.6	15	10.6	14	7.1	7.5	9.6	4.7	7.6	7.5	7.8	10	8.6
Goof	1.31	1.19	1.31	1.08	1.28	1.27	1.26	1.18	1.15	1.22	1.27	1.25	1.20	1.36
x (O)	0.2745 (7)	0.2741 (11)	0.273 (2)	0.275 (2)	0.278 (1)	0.2764 (8)	0.2779 (7)	0.2777 (9)	0.2779 (6)	0.2787 (9)	0.2795 (10)	0.2788 (10)	0.2779 (13)	0.2800 (10)
U_{Fe} (Å^2)	0.0062 (8)	0.0086 (10)	0.008 (1)	0.010 (1)	0.009(1)	0.0090 (8)	0.0092 (7)	0.0075 (8)	0.0093 (5)	0.0089 (6)	0.0092 (6)	0.0090 (10)	0.0098 (10)	0.0082 (9)
U_O (Å^2)	0.006 (1)	0.010 (10)	0.009 (2)	0.012 (2)	0.004 (2)	0.0101 (13)	0.0115 (11)	0.0095 (12)	0.0109 (7)	0.0091 (10)	0.0093 (11)	0.011 (2)	0.011 (2)	0.009 (2)

P#	P13	P14	P15	P16	P17_HS	P18_HS (*)	P18_LS	P19	P20	P20	P21	P22	P23	P24
Station	16BMD	16BMD	16BMD	16BMD	16BMD	16BMD	16BMD	16BMD	16BMD	16BMD	16BMD	16BMD	16BMD	16BMD
χ angle	χ b	χ a	χ a	χ a	χ a	χ a	χ a	χ a	χ b	χ c	χ a	χ a	χ a	χ a
P (GPa)	39.0 (2)	41.2 (2)	43.9 (1)	44.14 (9)	44.45 (6)	45.13 (9)	45.13 (9)	46.4 (1)	46.92 (10)	47.2 (2)	47.49 (6)	49.2 (2)	51.9 (2)	52.6 (1)
a (Å)	4.518 (2)	4.514 (2)	4.502 (2)	4.500 (2)	4.487 (3)	4.485 (2)	4.381 (10)	4.367 (2)	4.372 (2)	4.368 (2)	4.367 (2)	4.364 (2)	4.355 (2)	4.358 (2)
c (Å)	13.457 (12)	13.34 (2)	13.23 (2)	13.25 (1)	13.17 (2)	13.19 (1)	12.80 (5)	12.78 (2)	12.72 (1)	12.75 (1)	12.74 (2)	12.66 (2)	12.59 (1)	12.62 (2)
V (Å^3)	237.9 (4)	235.4 (6)	232.2 (6)	232.4 (4)	229.6 (7)	229.8 (4)	213 (2)	211.1 (5)	210.6 (4)	210.7 (4)	210.4 (5)	208.8 (5)	206.8 (4)	207.6 (5)
N_{all}	86	101	100	89		88		92	99	106	95	77	87	101
N_{ind}	29	31	31	27		31		32	31	35	30	24	29	29
R_{int}	6.7	8.5	12	15		5.7		8.2	4.2	5.9	7.3	6.3	17.3	3.6
R_{all}	4.9	4.1	4.8	5.2		3.7		3.5	2.2	2.7	2.8	2.3	4.5	2.8
wR2	7.4	8	9.5	12.3		8.8		8.3	5.2	6.1	6	6.1	11.3	6
Goof	1.33	1.28	1.28	1.25		1.31		1.21	1.20	1.08	1.25	1.17	1.24	1.16
x (O)	0.2780 (10)	0.278 (1)	0.2788 (13)	0.280 (1)		0.2811 (10)		0.2884 (8)	0.2892 (6)	0.2875 (6)	0.2885 (7)	0.2883 (8)	0.2890 (11)	0.2901 (10)
U_{Fe} (Å^2)	0.0106 (9)	0.0088 (9)	0.0091 (11)	0.007 (1)		0.0115 (10)		0.0059 (9)	0.0074 (6)	0.0041 (6)	0.0053 (7)	0.0055 (11)	0.0064 (12)	0.0070 (7)
U_O (Å^2)	0.011 (2)	0.010 (2)	0.012 (2)	0.005 (2)		0.009 (10)		0.0058 (12)	0.0080 (9)	0.0051 (9)	0.0058 (12)	0.007 (2)	0.004 (2)	0.008 (1)

P#	P24	P25	P26	P27	P27	P27	P27	P27	P27	P27	P28_LS	P28_HS	P29	P30
Station	16BMD	16BMD	16BMD	13IDD	13IDD	13IDD	13IDD	13IDD	16IDB	16IDB	16BMD	16BMD	16BMD	16BMD
χ angle	χ a-MI	χ a	χ a	χ a_CCD	χ b_CCD	χ c_CCD	χ c_CCD	MX_CCD	χ a	χ a_CCD	χ a	χ a	χ a	χ a
P (GPa)	52.6 (1)	54.0 (2)	55.96 (11)	55.0 (1)	55.0 (1)	55.0 (1)	55.0 (1)	55.0 (1)	55.0 (2)	55.0 (2)	41.0 (1)	41.0 (1)	36.2 (1)	14.20 (7)
a (Å)		4.355 (2)	4.343 (2)	4.3474 (12)	4.3462 (11)	4.3480 (10)	4.3480 (10)		4.347 (1)		4.37 (2)	4.507 (5)	4.532 (2)	4.604 (3)
c (Å)		12.54 (1)	12.497 (11)	12.534 (8)	12.519 (10)	12.52 (1)	12.52 (1)		12.477 (12)		12.82 (5)	13.23 (3)	13.45 (1)	14.519 (10)
V (Å^3)		205.9 (4)	204.1 (4)	205.2 (2)	204.8 (3)	205.0 (3)	205.0 (3)		204.2 (3)		212 (3)	232.7 (10)	239.2 (4)	266.5 (5)
N_{all}	108	102	126	77	79	83	83	185	101	98				
N_{ind}	31	33	39	28	24	29	29	32	28	24				
R_{int}	5.8	3.7	9.1	9.7	9.3	6.1	6.1	10.2	9.3	18				
R_{all}	2.7	2.4	4.0	4.2	3.5	4.0	4.0	3.1	3.1	5.04				
wR2	4.4	5.7	7.7		6.9	6.5	6.5	6.2	7.4	6.5				
Goof	1.22	1.38	1.12	1.21	1.17	1.33	1.33	1.26	1.23	1.14				
x (O)	0.2878 (6)	0.2898 (7)	0.2901 (8)	0.2887 (9)	0.2904 (11)	0.2886 (7)	0.2886 (7)	0.2899 (6)	0.2896 (10)	0.2915 (7)				
U_{Fe} (Å^2)	0.0062 (5)	0.0075 (7)	0.0053 (7)	0.010 (1)	0.0078 (10)	0.0096 (9)	0.0096 (9)	0.0096 (8)	0.007 (1)	0.0084 (8)				
U_O (Å^2)	0.0051 (8)	0.009 (1)	0.0047 (10)	0.011 (1)	0.009 (1)	0.0093 (12)	0.0093 (12)	0.0107 (10)	0.009 (1)	0.0081 (12)				

Table II: Lattice parameters and results from structural refinements. Refinement at some pressures were not performed due to peak splitting or incomplete dataset. Label in the first row indicate the pressure step, in the second row the experimental station is reported (see text) in the third row the χ angle (χa=0º, χb ≈30º, χc≈60º) at which the rotation image was taken. Other labels indicate: CCD: MARCCD detector used instead of MAR345IP; MI: refined intensities were extracted from images with different exposure time, scaled and merged; Mχ: intensities from exposures at different angle were rescaled and merged. N_{all}, N_{ind}: total number of reflections used in the refinement and symmetry independent respectively. R_{int}, R_{all}, wR_2, Goof: statistical parameters of the structural refinement [18]. x(O), U_{Fe}, U_O: refined oxygen fractional coordinate, and isotropic displacement parameters of Fe and O atoms respectively. (*) only the HS component of the peaks was integrated for the structural refinement.